JOM, Vol. 77, No. 8, 2025
https://doi.org/10.1007/s11837-025-07361-8

The Influence of Convection and Iron Content on the Solidification Microstructure of Technical Aluminum Alloys

GOLO ZIMMERMANN ,[1,4] ANGELOS THEOFILATOS,[3] SONJA STEINBACH,[2] ALEXANDRE VIARDIN,[3] LASZLO STURZ,[3] and FLORIAN KARGL[1,2]

1.—RWTH Aachen University, Foundry Institute, Intzestraße 5, 52072 Aachen, Germany. 2.—Institut für Materialphysik im Weltraum, Deutsches Zentrum für Luft- und Raumfahrt (DLR), Linder Höhe, 51170 Köln, Germany. 3.—ACCESS e.V., Intzestr. 5, 52072 Aachen, Germany. 4.—e-mail: g.zimmermann@gi.rwth-aachen.de

In this work, two different variants of image segmentation are compared to evaluate the use of generalized machine learning models against the accuracy of bespoke models to further their use for the analysis of microstructure images with multiple phases. The results from the analysis are then used to evaluate the effect of different iron contents and the presence or absence of convection on the formation of the microstructure with emphasis on the development of the intermetallic phases in technical aluminum alloys. To this end, the study focuses on aluminum-silicon base cast alloys with high iron content directionally solidified under microgravity conditions, with additional controlled convection created by a rotating magnetic field. Optical microscopy images from the different processing zones are then used to train the different chosen models, which are afterwards used to segment and analyze the microstructures. Key results include the evaluation of the effects of convection and iron content on several parameters describing the different intermetallic phases as well as the comparison of the models.

INTRODUCTION

Recycled aluminum alloys are playing an increasing role in the manufacturing industry.[1] To better understand the influence of composition changes on the alloys' microstructure, a study of the effects on its components is required. The changes include the enrichment of some elements only present in low amounts in the primary alloys. For example, iron is an element with an average concentration of 0.07–0.10 wt% in aluminum cast alloys. Remelting cycles during recycling lead to an increase in concentration that can lead to iron contents of up to 1.5 wt% in alloys for high-pressure die casting.[2] These increased amounts of iron further the formation of iron-containing intermetallic phases, for example, α-Al_8Fe_2Si or β-$Al_9Fe_2Si_2$,[3] or change the formation processes of these or other intermetallic phases.[2,4] With these changes, an impact on the mechanical properties must be expected. Furthermore, changes in the solidification behavior of the intermetallic phases can also impact the overall processing and solidification of the melt because of the formation of phase networks or other three-dimensional structures and their interaction with the dendritic network.[5] This necessitates the analysis of the impact of changes in melt flow behavior on the microstructure as always present in casting processes. The analysis of the microstructure can be a time-consuming process due to the long sample preparation and measurements.[6] While reducing the duration of sample preparation is difficult, the measurements and analysis performed on the microstructural components have high potential for automation due to the advancements in image analysis techniques.[7–9] The introduction of

(Received January 31, 2025; accepted March 19, 2025; published online April 10, 2025)

automated processes, using machine learning tools, for example, still requires optimization of the models used for the analysis to improve the model accuracy, speed of application and training, as well as the ease of use.

In this work, an advanced machine learning algorithm called Mask R-CNN (Mask Region-based-Convolutional Neural Network),[10] trained for broad applicability, is compared with the results of simpler bespoke models trained on a per-image basis using the random forest algorithm. This algorithm is implemented in the Weka Segmentation plugin[11] in Image J.[12] The differentiation between bespoke and broadly applicable models refers to the impact of the respective training database. For the bespoke models, the training is conducted using a large fraction of a single image. This makes applying the model outside of the training image very unreliable but allows for the full segmentation of that image. The broadly applicable model, on the other hand, uses a wide variety of training images and can therefore be used to segment a diverse set of similar images in the end. The methods are evaluated on two aluminum alloys with increased iron content, solidified under microgravity conditions onboard the International Space Station (ISS) in the European Space Agency's (ESA) Materials Science Laboratory (MSL) within the frame of the ESA-project MICAST[13] with convection induced using a rotating magnetic field. The alloys are the hypoeutectic Al-6 wt% Si-4 wt% Cu-1 wt% Fe (MICAST 3#3), for which β-$Al_9Fe_2Si_2$ phase precipitates after primary α-Al, and the hypereutectic Al-6 wt% Si-4 wt% Cu-2 wt% Fe (MICAST 3#5), for which α-Al_8Fe_2Si phase precipitates first, followed by primary α-Al. Besides evaluating the model training and performance, the focus here is on analyzing the influence of convection and iron content on the size and positioning of the phases present in the microstructure.

EXPERIMENTAL SETUP AND SAMPLE ANALYSIS

MSL's Bridgman-type furnace insert SQF (solidification and quenching furnace; moving furnace, static sample) was used to directionally solidify the rod-like samples with a length of 276 mm and a diameter of 7.9 mm. The furnace is equipped with a coil system capable of generating a rotating magnetic field for electromagnetic stirring of the liquid sample during processing.[4,13] For the processing, the solidification velocity was held constant at 0.04 mm/s with a temperature gradient between 2.25 K/mm and 2.5 K/mm. During processing under convective conditions, the magnetic field operated with a frequency of 57 Hz and a field strength of 5.7 mT, inducing a laminar melt flow.[5] To create two processing zones during solidification, one solidifying under pure diffusive mass transport conditions and the other under forced convection in microgravity, the magnetic field was switched on after a traversal of 70 mm by the furnace. The furnace continued movement till 150 mm without stopping. During the analysis of the process data, the positions of the processing zones were determined with three-dimensional polynomial models over time, position and temperature measured by 12 thermocouples within the sample cartridge. The models were inverted using the isothermal temperatures for the potentially occurring phases given in Table I and the coordinates for the processing zones calculated. For solidification under microgravity, the conditions were that at the initialization of the magnetic field the phase with the lowest melting point (Al_2Cu; Table I) had already completely solidified after being fully melted at some point during the process. For the zone that solidified under convective conditions, the prerequisite was that the sample area had to be fully liquid at initialization of the magnetic field.

The samples were extracted as axial cross-sections using a Buehler IsoMet High Speed Pro Precision Cutter and ground and polished to 0.05 μm using a SiC polishing solution. Mosaic images for analysis were taken using a Zeiss microscope (Axio Imager A2m). Observation was focused on the β-$Al_9Fe_2Si_2$ intermetallic phases (IMP), the silicon particles from the Al-Si eutectic and the Al_2Cu phase occurring in the samples. The phase composition was confirmed using a scanning electron microscope.

To simplify some of the planned measurements and reduce the data load during model training, the analyzed area of the cross-sections was restricted to a horizontal rectangular section, as shown in Fig. 1. Since the full images show an agglomeration of intermetallic phases in the center of the sample, but the restricted area precludes the full use of the vertical axis, changes to the description of this agglomeration are required. The determination of the position of the analyzed microstructure components therefore only considered the horizontal deviation from the center of the sample, with the center being represented by the x-component of the full samples focal point. The low estimated impact of the vertical y-axis in the restricted sample area used for the measurements makes this change feasible.

Training of the Random Forest Models

The training of the models for the initial segmentation of the sample images was conducted on the extracted image sections, an example of which is shown in Fig. 2. The figure also includes marked regions in red for the second segmentation method. The models for the first segmentation method were trained using the Weka Segmentation plugin in the Fiji implementation of Image J. The chosen training features were Gaussian Blur, Hessian, Mean, Sobel Filter, Difference of Gaussians and Bilateral. Further information on these training features can be

Table I. Isothermal temperatures used in the determination of the processing zone positions according Thermo-Calc (TCAL5 database)

Phase	AlSi6Cu4Fe1 (hypoeutectic) temperature (°C)	AlSi6Cu4Fe2 (hypereutectic) temperature (°C)
α-Al_8Fe_2Si	–	628
α-Al	610	608
β-$Al_9Fe_2Si_2$	602	603
eutectic Al-Si	561	559
Al_2Cu	522	521

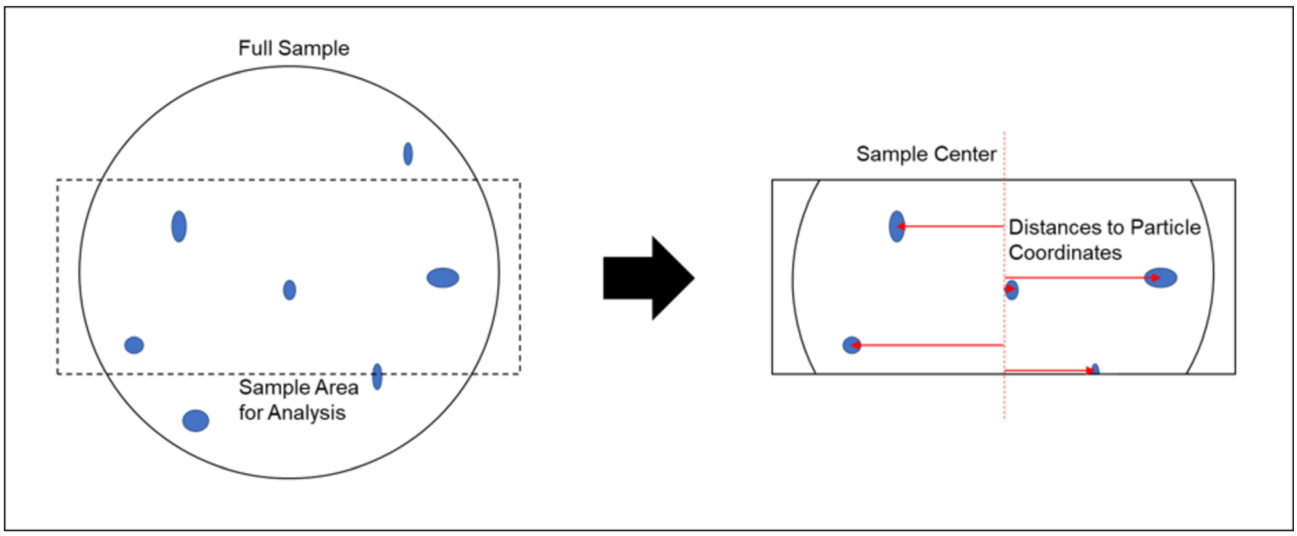

Fig. 1. Schematic of the area selection method for later analysis (left) and of the measurement method of the particle distance to sample center (right, sample diameter 8 mm).

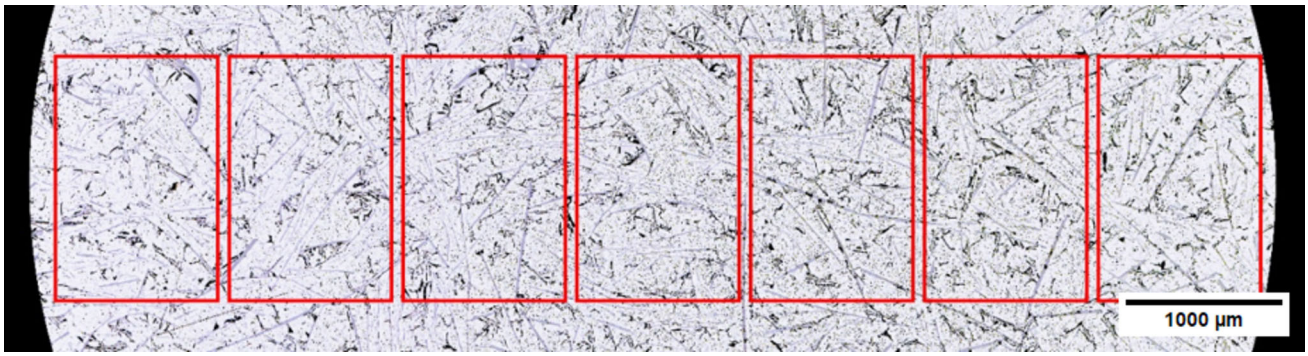

Fig. 2. Selected section of the microstructure of MICAST 3#3 solidified under μg conditions, sample 2 (sample diameter 8 mm). Regions marked in red are used in the second segmentation method (box size 1000 $\times$ 1500 pixels) (Color figure online).

found in the plugin documentation. As classes for the model, all recognizable features of the microstructures were used: aluminum matrix, silicon particles, β-$Al_9Fe_2Si_2$ particles, Al_2Cu particles and a background for sample surroundings and random defects or image artifacts.

A single, bespoke model was created for each image. This allowed for the segmentation of the full microstructure in one classification. A result of a segmentation is shown in Fig. 3. After the segmentation, a median filter with a 2-pixel radius was applied to the images to eliminate thin artifacts and classification errors at the edges of the components of the microstructure, especially of the β-$Al_9Fe_2Si_2$ particles. This is necessary since the coloration of the phases often differs at the edges because of the polishing process, which leads to classification errors. These show as thin, wrongly classified outlines. The median filter recolors pixels in the predominant color in a small radius,

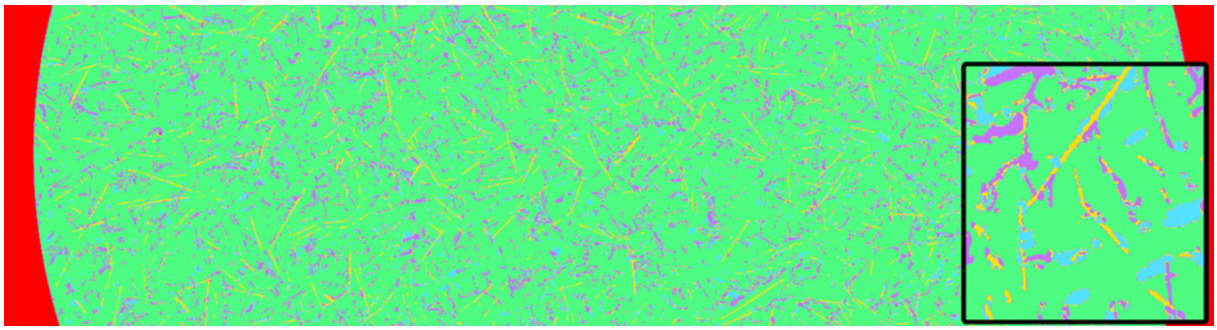

Fig. 3. Segmented microstructure of MICAST 3#3 solidified under μg conditions sample 2 (sample diameter 8 mm); colors correspond to the available phases as follows: red = background or holes, green = aluminum matrix or dendrites, violet = silicon from the eutectic, yellow = β-$Al_9Fe_2Si_2$ phase, blue = Al_2Cu; the right side of the image includes a zoomed-in view of one image section (Color figure online).

eliminating the outlines and other small artifacts. Afterwards, the segmented and corrected images were used to create binary versions, one each for Si, Al_2Cu and β-$Al_9Fe_2Si_2$ particles. These binary versions were then used to extract positions, distances and shape descriptors for all particles. During the measurements, particles composed of < 30 pixels were excluded because of the high probability of errors, the low quality of extractable shape descriptions and the low impact on measurable overall area.

Training of the Mask R-CNN Model

The light optical microscope (LOM) images of the samples demonstrate a microstructure consisting of the matrix phase and three distinct precipitate phases. These phases can be distinguished from each other by their characteristic shape and color (Fig. 2).

- The Al-matrix, considered the background, has a light gray-white color. Small dark spots consist of SiO_2 and are introduced during the metallographic preparation; they are ignored in further analysis.
- The β-$Al_9Fe_2Si_2$ phases have a characteristic elongated needle-like shape in 2D and a light-grey to dark-grey color.
- Eutectic silicon (Al-Si) has an irregular, faceted shape and a very dark gray to black color.
- Finally, the Al_2Cu phase is characterized by a light red color. Its saturation strongly depends on the sample preparation and microscopy procedure, resulting in variability across images. This phase exhibits an irregular morphology, ranging from round globules to small, elongated colonies. This phase can often be observed attached to Al-Fe-Si needles or to eutectic Si. Due to its inconsistent shape and color, its identification by the AI model has not been considered reliable and thus has not been reported.

Dataset Generation

For the generation of the training dataset, neutral background images were generated, with a color scale analogous to the Al matrix. To simulate the SiO_2 particles, porosity and general image noise, additional random noise was introduced to the generated background images. From the LOM images, approximately 100 particles from each phase were extracted (see Fig. 4), selected from all four experimental series MICAST 3#3 (μg and RMF), as well as MICAST 3#5 (μg and RMF). The dataset was then generated by randomly overlapping cropped particle images on the background images. For each cropped image that was overlaid, the pixels corresponding to it were stored as a mask and the bounding box was calculated. The respective data were stored in a JSON file in the COCO format.

Training and Inference

Two distinct models were trained for the LOM images: one for the eutectic Al-Si phase and another for the Al-Fe-Si phase, both using 100–120 features per image. For the training of each phase, 5000 training images and 500 validation images were generated. The training was restricted to 30 epochs to avoid overfitting. The intersection over the union threshold was kept at 0.5 during training and 0.7 for inference, while the score threshold was kept at 0.01 (training) and 0.05–0.1 (inference). Both thresholds were kept low during the training to enhance detection of smaller features and generalization.

Contour Analysis

The eight rectangular cross-sections (two cross-sections from the sample part solidified without and two cross-sections from the sample part solidified under convective conditions, for each of the two sample rods) were divided into seven images (see Fig. 2) with dimensions of 1000×1500 pixels each, exemplarily shown in Fig. 2, and then loaded to the trained model for the detection of the two phases. The contours of the detected phases were exported and loaded for further analysis. A minimum size threshold of 5 pixels was used to filter out noise and incorrect detections. Subsequently, the detected contours underwent a further refinement, during

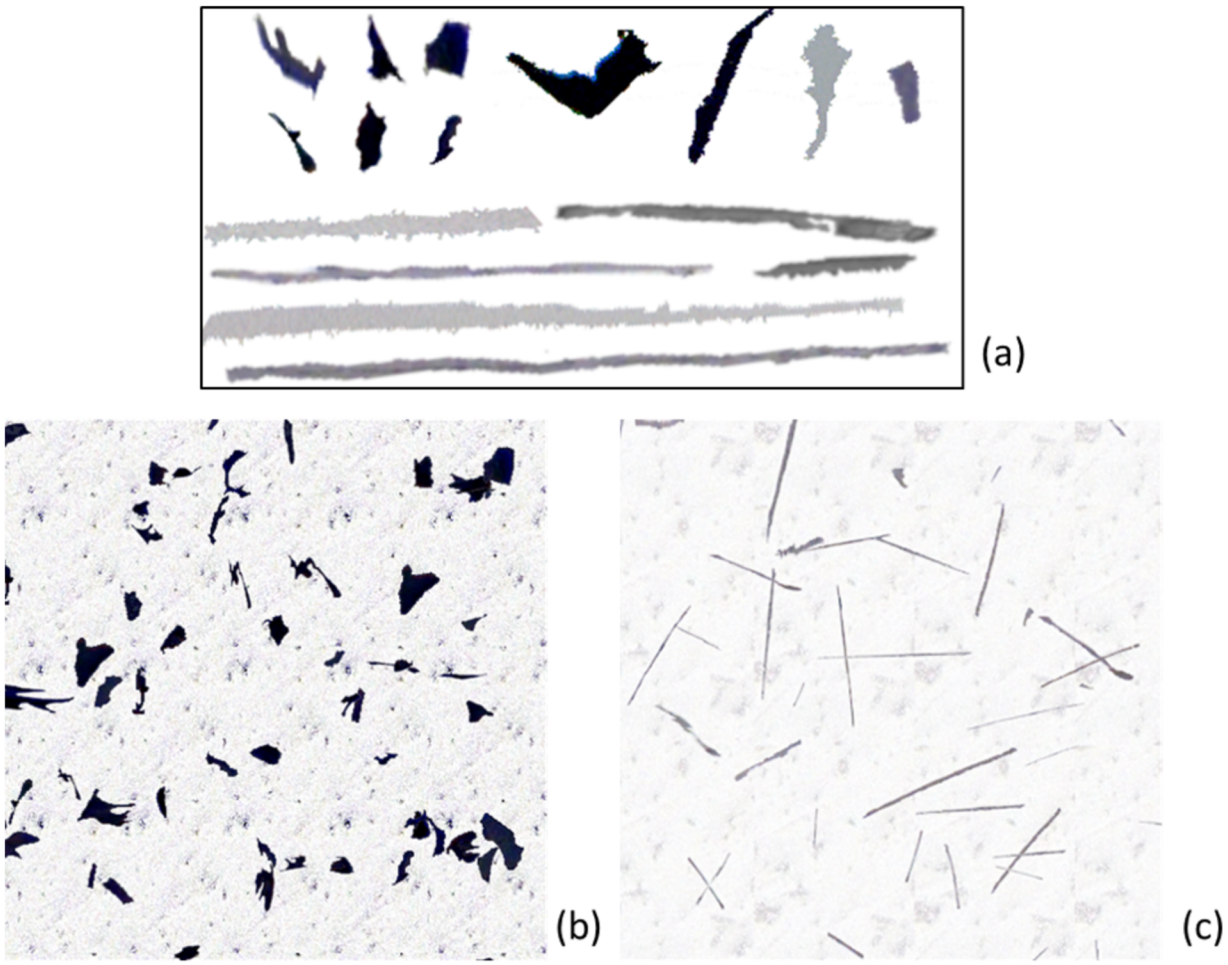

Fig. 4. Features from all eight base images were cropped and overlaid on a neutral background resembling the aluminum matrix. Image (a) on top illustrates examples of eutectic Al-Si features and needle-like Al-Fe-Si features after cropping. The lower images (b) and (c) show two examples of training images, one for each phase.

which detections exhibiting an overlap > 35–80% were excluded from further analysis, and only the contour with the biggest area was kept.

The Feret diameter was calculated by measuring the pairwise distance of all points of each individual contour. Subsequently, two lines were generated: one connecting the two points and one 90° rotated from the former. The latter was shifted to pass through the geometric center of the contour. The minimum Feret diameter was calculated by measuring the projected distance of the contour points on the second line. Finally, the geometric centers of the contours were used to calculate their distance from the center line of the rectangular section, as well as the distance to the nearest neighbor (NND), between the same phases and the two different phases.

RESULTS AND DISCUSSION

Analysis of the Microstructure from Random Forest Segmentation

The analysis of the microstructure focuses on a limited set of parameters. Because the Si-particles and the β-$Al_9Fe_2Si_2$ particles both mostly have a needle-like shape, the Feret diameter and minimum Feret diameter, so the maximum and minimum diameters of the analyzed particles, were chosen to represent the particle shape. These align with a needle or plate section length and width. Additionally, the position of the particles is represented by the horizontal distance from the sample center, while the positional relation of the particles can be shown using the distance to the nearest neighbor of the specified type of particle. Where shown, the standard deviation can be used to estimate the uniformity of a distribution of measurements. All chosen parameters are evaluated based on the base alloy, specifically the changes in iron content from 1 wt% to 2 wt%, and based on the change in processing from solidification in microgravity to being influenced by the rotating magnetic field.

The results of the measurements for the Feret diameter and the distance from the sample center are shown in Fig. 5. For the MICAST 3#3 alloy with 1 wt% iron, the influence of the rotating magnetic field, and therefore convective conditions during

solidification, on the average distance from the sample center is most pronounced. The average distance for all observed phases decreases significantly from processing under diffusive conditions to processing under convective conditions. For the alloy with 2 wt% iron (MICAST 3#5), an increase in average distance is seen for silicon and Al_2Cu phases, while the distance stays mostly constant, the average showing only a very slight decrease, for β-$Al_9Fe_2Si_2$. Regarding the influence of the iron content, the comparison of the values for microgravity conditions is more promising, since the magnetic field has such a pronounced influence on the MICAST 3#3 alloy. The increase in iron content leads to an increase of the average distance from the sample center for the β-$Al_9Fe_2Si_2$ phase but to a smaller decrease for Si and Al_2Cu. For the Feret diameter, the influence of convection created by the rotating magnetic field leads to a small increase at 1 wt% iron for β-$Al_9Fe_2Si_2$ and Si but to a slight decrease for Al_2Cu. At 2 wt% iron, a clear decrease of the Feret diameter is seen for β-$Al_9Fe_2Si_2$ and a small increase for both other phases. Under the same processing conditions, the increase in iron content leads to a large increase of the Feret diameter for the β-$Al_9Fe_2Si_2$ phase. This increase is somewhat less pronounced under convective conditions.

Overall, the observations align with qualitative observations of changes in the microstructure that can be made directly from the images: The fluid flow structure induced by the RMF leads to a strong macro-segregation.[5] The swirl flow in the bulk liquid induces a flow motion inside the mushy zone. The upward-directed interdendritic flow transports solutally enriched liquid out of the two-phase region at the axis of the sample. Consequently, a solute-enriched channel develops inside the mushy zone. A coarsened zone of β-$Al_9Fe_2Si_2$ and Si in the sample center for the samples with 1 wt% iron is formed; 2 wt% iron leads to more and larger β-$Al_9Fe_2Si_2$ phases, which form a three-dimensional network throughout the samples. This network, presumably caused by the generally increased fraction of Fe-containing phases and the occurrence of a second Fe-based intermetallic phase, changes the flow conditions early on during solidification and thus prevents the channel formation for the samples with 2 wt% iron. In addition, the primary dendrite arm spacing, as reduced by the influence of the RMF,[14] leads to a reduction in the average size of β-$Al_9Fe_2Si_2$ particles, since they are smaller because of the reduced space to grow.

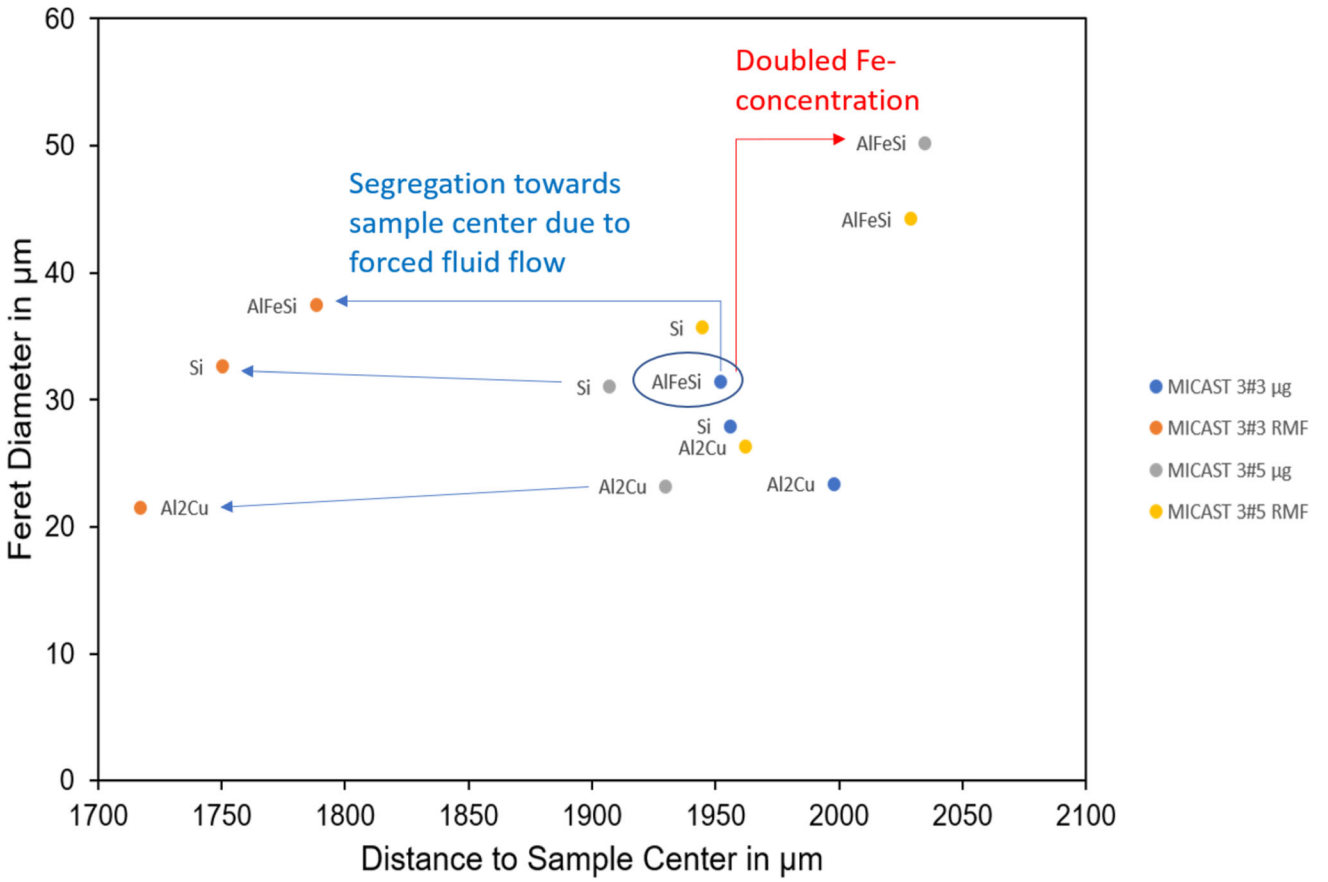

Fig. 5. Feret diameter over the distance from the sample center for three microstructure components in AlSi6Cu4 alloys with 1 wt% (MICAST3#3) and 2 wt% (MICAST 3#5) iron, samples solidified in microgravity and under influence of a rotating magnetic field.

The standard deviation for the Feret diameter, as shown in Fig. 6, generally follows the observations from the average values and can be used to support the findings made there. The decrease in the shown values for 2 wt% iron due to the influence of convective processing is very pronounced for the β-$Al_9Fe_2Si_2$ phase and can therefore be used to draw the conclusion that the processing conditions lead not only to a phase size reduction but also to a homogenization with more uniform β-$Al_9Fe_2Si_2$ particles being formed during the primary solidification.

The minimum Feret diameter, again plotted over the distance from the sample center, is shown in Fig. 7. Generally, a low impact of the processing conditions can be observed for the Al_2Cu and β-$Al_9Fe_2Si_2$ phases. For the Si phases, an increase due to convection is measurable for 1 and 2 wt% iron. Together with the previously noted increase in the (maximum) Feret diameter for the Si particles, this points to an overall enlargement being caused by the formation of a solutally enriched channel due to the RMF (enrichment of Si). The decrease in the minimum Feret diameter for the β-$Al_9Fe_2Si_2$ phase at 2 wt% iron caused by the onset of convective flow can probably be attributed to the size reduction also observed for the needle or plate length. The increase of the iron content causes an increase of all minimum Feret diameters, besides for β-$Al_9Fe_2Si_2$ under convection. There a decrease is observable.

The positional relation of the phases to each other and the influence of processing and composition on it can be analyzed using the nearest neighbor distance (NND). A distinction is made here between the distances within particles of one phase, shown in Fig. 8, and the distances between the different phases, shown in Fig. 9. For the same phase, the influence of the change from microgravity to convection at 1 wt% iron leads to an increase of the NND for Si and β-$Al_9Fe_2Si_2$ and a decrease for Al_2Cu. At 2 wt% iron, the NND for Si-particles stays constant and increases for Al_2Cu while decreasing for β-$Al_9Fe_2Si_2$. The influence of the iron concentration is marked by an increase of all NNDs by varying degrees under microgravity conditions with rising iron content (very small for Al_2Cu). This increase of the NND is still observable under the influence of the rotating magnet field for the Al_2Cu particles but mostly absent for Si and β-$Al_9Fe_2Si_2$.

The distances between the different phases are split into three different combinations: β-$Al_9Fe_2Si_2$ to Si (β-$Al_9Fe_2Si_2$ being shortened to FeSi in the graph), β-$Al_9Fe_2Si_2$ to Al_2Cu and Si to Al_2Cu. All combinations can be analyzed in the same categories as in the previous figures. The nearest neighbor distance from β-$Al_9Fe_2Si_2$ to Si increases from microgravity to convection for the alloy with 1 wt% iron and slightly decreases at 2 wt% iron. An increase in iron content always leads to an increase in the NND, regardless of the processing. For the distance between β-$Al_9Fe_2Si_2$ and Al_2Cu particles, the NND stays almost constant (1 wt%) or increases (2 wt%) when introducing convection. The behavior regarding the change in iron content again always

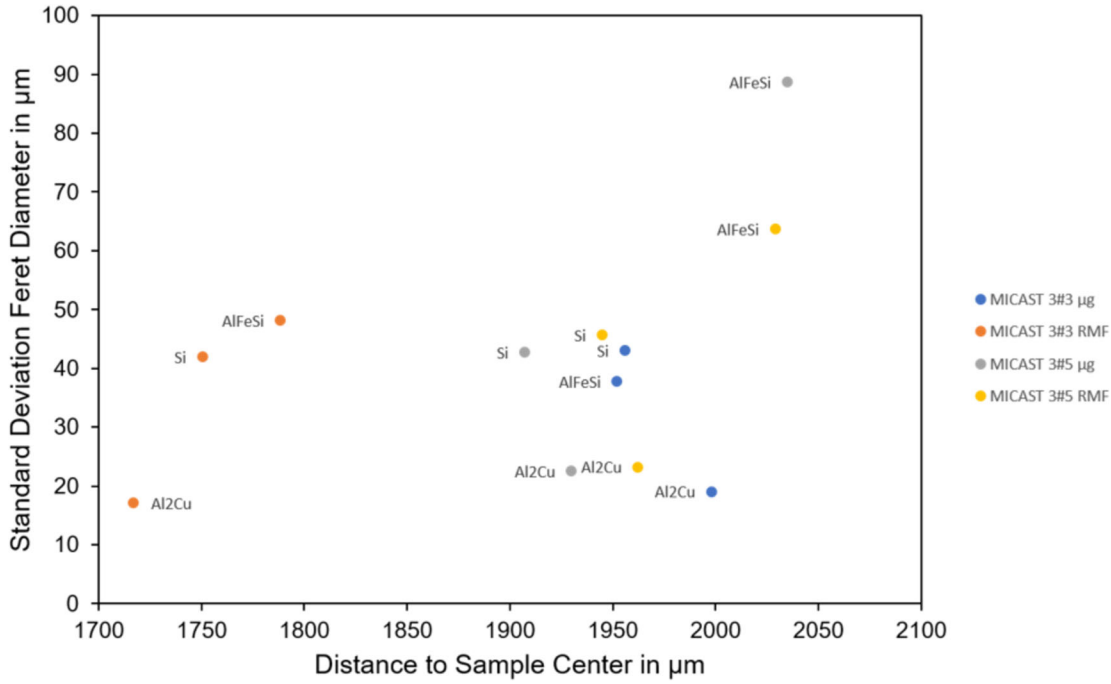

Fig. 6. Standard deviation of the Feret diameter over the distance from the sample center for three microstructure components in AlSi6Cu4 alloys with 1 wt% (MICAST3#3) and 2 wt% (MICAST 3#5) iron; samples solidified in microgravity and under the influence of a rotating magnetic field.

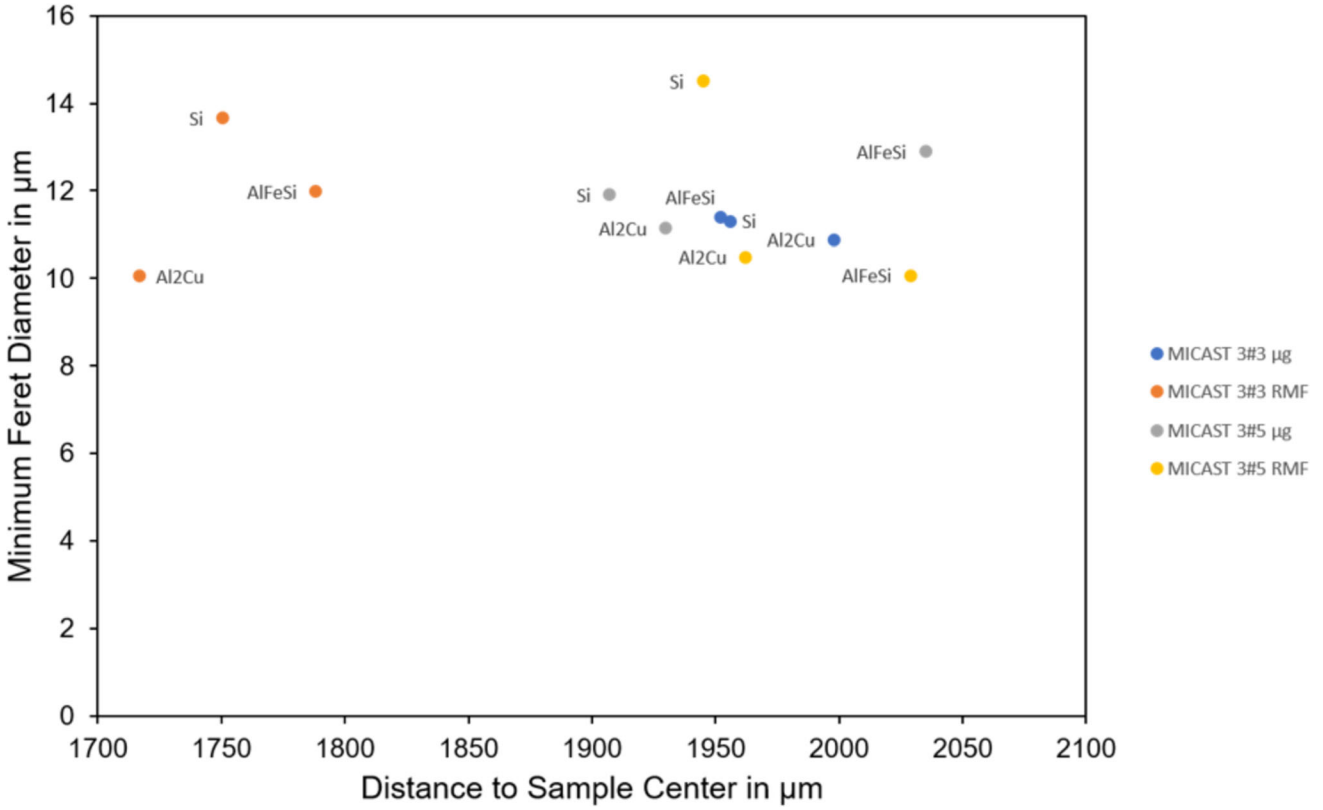

Fig. 7. Minimal Feret diameter over the distance from the sample center for three microstructure components in AlSi6Cu4 alloys with 1 wt% (MICAST3#3) and 2 wt% (MICAST 3#5) iron samples solidified in microgravity and under the influence of a rotating magnetic field.

shows an increase in the NND for the higher iron content. Last, the distance between Si and Al_2Cu shows a small decrease for 1 wt% iron and an increase for 2 wt% in change to convective processing. The influence of the iron content is visible in a very low increase of the NND under microgravity and significantly evident in a clear increase with an active rotating magnetic field. The almost constant NND for Si to Al_2Cu under microgravity is the outlier in behavior here since, in all other cases, the increase in iron content leads to an increase in the NND as well.

Most effects on the NND observed in this study remain relatively small, with a notable exception for the effect increasing the iron content has on the distance between β-$Al_9Fe_2Si_2$ and Si solidified under microgravity. The large increase in the distance measured there can probably be partly attributed to the effect of the measurement method, which determines the NND by measuring the distance between the particle centers. This method leads to larger NNDs for larger particles. With the increase in β-$Al_9Fe_2Si_2$-size, unconstrained by the effects of the inactive RMF, this effect is therefore expected. Less pronounced, it can also be observed for the distance to Al_2Cu. This difference can be attributed to the growth behavior of the different phases, with Al_2Cu often being observed growing on or near the β-$Al_9Fe_2Si_2$ phase.

Analysis of the Microstructure from Mask R-CNN Segmentation and Comparison

The AI model demonstrated high reliability in detecting most of the features present in the images. Improvements can still be achieved by implementing additional post-processing steps. For example, the detections could be further refined by removing overlapping detections, noise and multiple detected features. An issue that was identified is the combination of crossing contours with minimal overlap. Specifically, the elongated needle-like structure of the Al-Fe-Si phase allows the crossing of the needles, which results in a detection of the combined area of the needles. This leads to increased average Feret diameters, as illustrated in Table II. Additional conditions can be implemented to differentiate between the crossing needles; however, this was not within the scope of this study. This issue does not arise in the case of the eutectic Al-Si phase because of its smaller size. Another issue with the detection is the low width of the particles, particularly the Al-Fe-Si needles (shown in Fig. 10), which are often only a few pixels thick. These cannot be reliably detected. A solution for this problem, presumably at the cost of the overall measured area, would be using higher-resolution images made at a higher magnification.

The measurements derived from the AI model are in good proximity to the outcome of the Weka

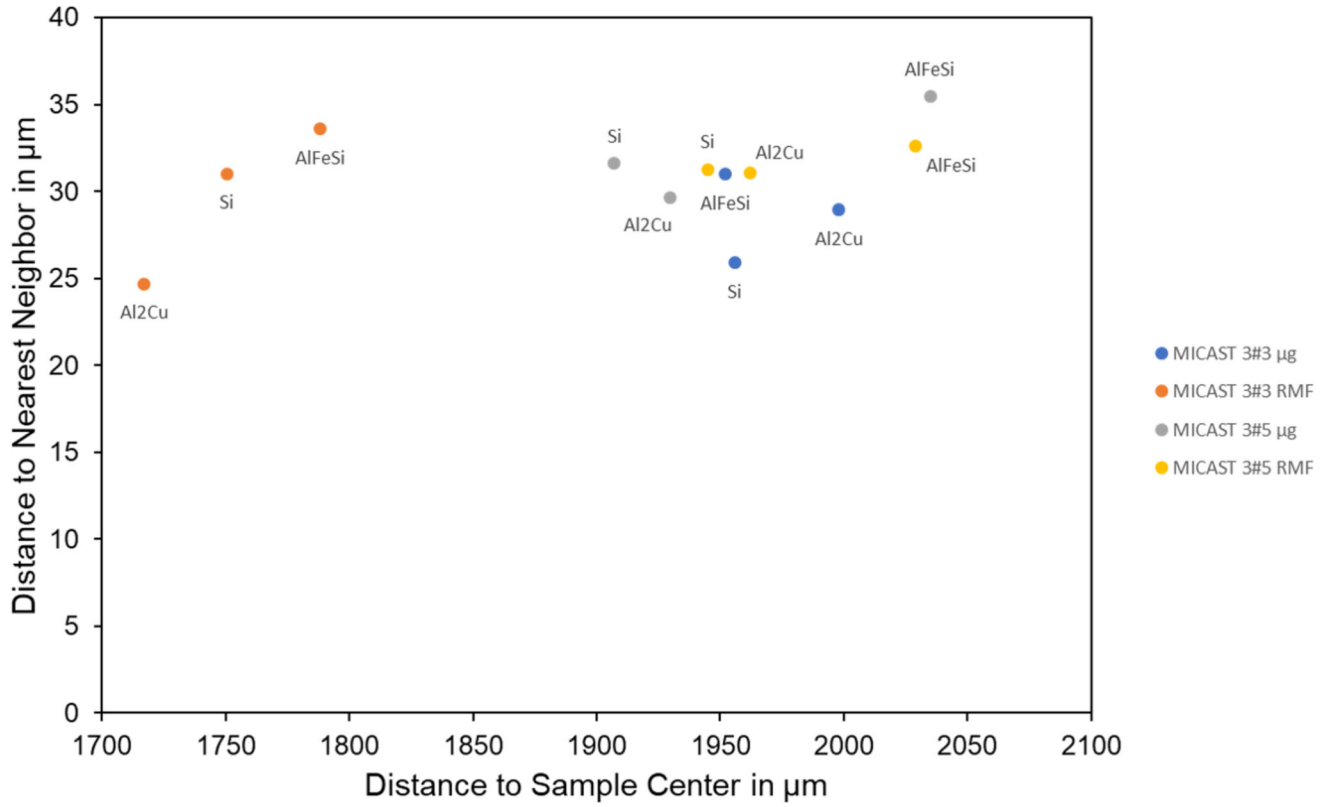

Fig. 8. Distance to the nearest neighbor of the same phase over the distance from the sample center for three microstructure components in AlSi6Cu4 alloys with 1 wt% (MICAST3#3) and 2 wt% (MICAST 3#5) iron, samples solidified in microgravity and under the influence of a rotating magnetic field.

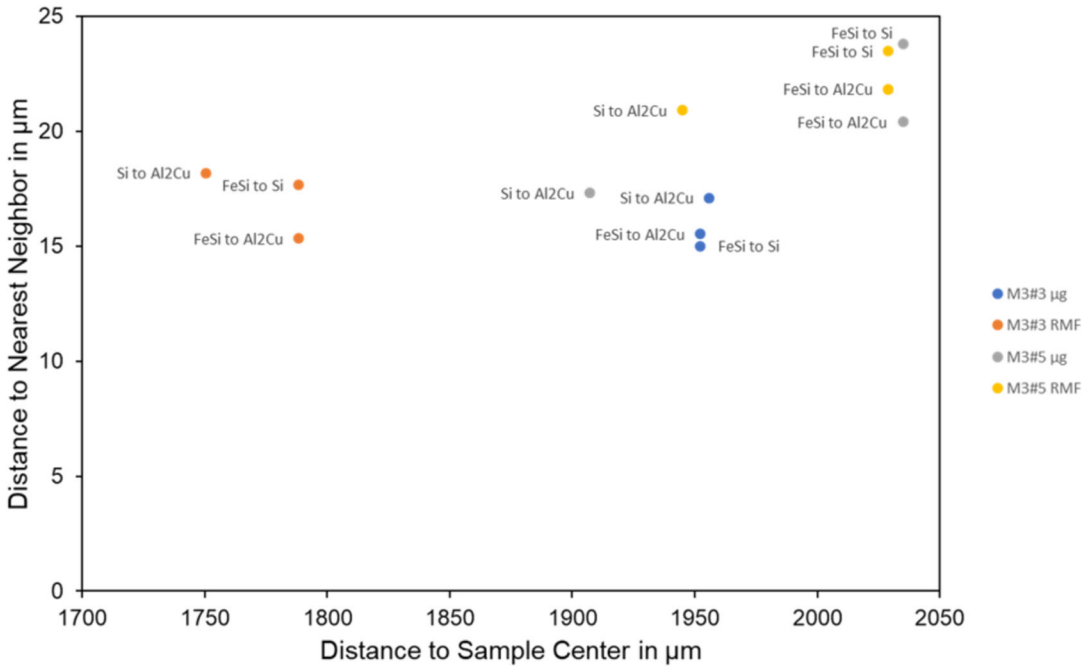

Fig. 9. Distance to the nearest neighbor of a different phase over the distance from the sample center for three microstructure components in AlSi6Cu4 alloys with 1 wt% (MICAST3#3) and 2 wt% (MICAST 3#5) iron, samples solidified in microgravity and under the influence of a rotating magnetic field.

Table II. Comparison of the microstructure parameters for the different segmentation models

	M3#3 µg		M3#3 RMF		M3#5 µg		M3#5 RMF	
	AI	**Weka**	**AI**	**Weka**	**AI**	**Weka**	**AI**	**Weka**
Eutectic Al-Si								
Distance (µm)	1853.14	1955.93	1770.22	1750.41	1818.65	1907.19	1930.49	1944.85
Feret diameter (µm)	31.97	27.89	35.59	32.60	31.19	31.01	33.02	35.66
Min. Feret (µm)	10.65	11.30	16.33	13.67	13.02	11.90	11.00	14.51
NND (µm)	27.06	25.91	30.67	31.03	28.07	31.61	33.76	31.27
Al-Fe-Si								
Distance (µm)	2067.77	1952.09	1884.35	1788.27	1907.17	2034.92	2047.33	2028.98
Feret diameter (µm)	35.32	31.44	66.44	37.42	87.09	50.22	81.24	44.24
Min. Feret (µm)	10.38	11.40	12.90	11.98	12.04	12.90	12.89	10.07
NND (µm)	31.35	31.01	58.60	33.59	31.79	35.46	46.27	32.63
AlFeSi-AlSi								
NND (µm)	51.07	15.01	53.82	17.65	46.47	23.80	48.81	23.49

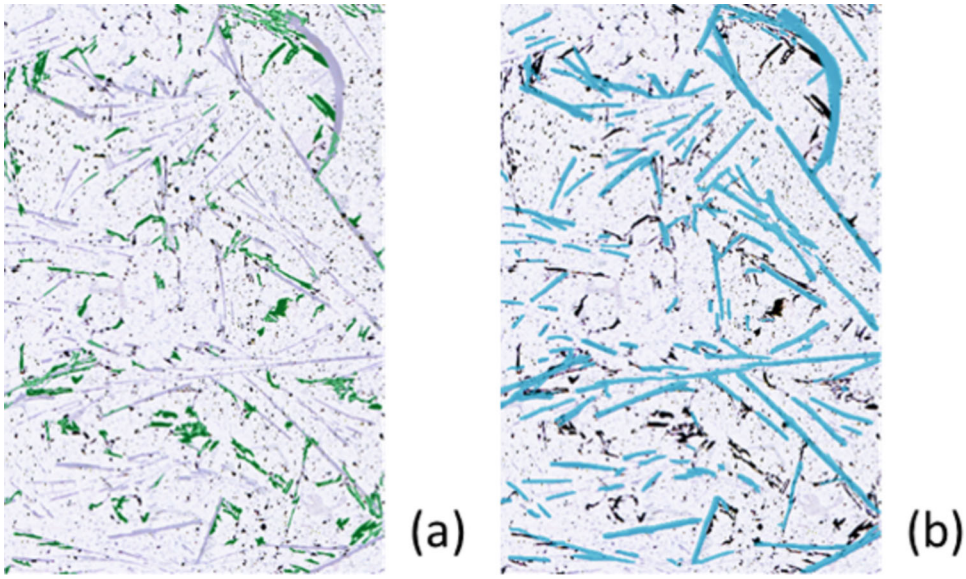

Fig. 10. Inference results for the first ROI in Fig. 2. The left image shows the identified features corresponding to the eutectic Al-Si phase and the right one for the Al-Fe-Si phase. The difference in the morphology of these two phases can be clearly observed.

method, as illustrated in Table II. The discrepancies between the Weka measurements and the AI-produced measurements can be attributed to the challenges mentioned above. First, smaller detections are not consistent using the AI method. Second, separating different needles further increases the computed average size.

The primary benefit of the AI model over conventional image analysis methods is the capacity to differentiate individual particles and features in an automated manner. Additionally, this automated process chain, starting from the trained model, can be used for all similar LOM images, with minimal interference.

CONCLUSION

The presented study showed the effect of introducing convective melt flow during solidification on the microstructure, particularly the intermetallic phases. Additionally, the differences in the effects with 1 wt% and 2 wt% iron could be compared. Overall, a few pronounced effects are visible.

- Regarding the distance from the sample center, the introduction of convection leads to a reduction due to the formation of a solute-enriched channel in the sample center[5,14] as long as the IMPs do not form a full three-dimensional network within the sample.

- At high iron content, convection leads to a size reduction of the iron-containing IMPs, which are otherwise much larger when solidified in microgravity because of the iron concentration.
- Regarding the distances between the different phases, the most pronounced effect could be observed for the distance between β-$Al_9Fe_2Si_2$ and the eutectic Si, which increases significantly for higher iron content under microgravity.

The comparison of the different models used for image segregation shows that using generalized models leads to comparable results to the bespoke models, with further possibility to improve the results by model refinement, improvements and standardization of sample preparation and image acquisition, especially regarding the Al_2Cu phase, and further introduction of more varied training data.

ACKNOWLEDGEMENTS

The KIMi team (BMWK/DLR research project Künstliche Intelligenz analysiert Mikrostrukturen) gratefully acknowledges financial support from BMWK under contract 50WM2356A and 50WM2356B. This work was supported by the ESA team MICAST AO-99-031 (MIcrostructure Formation in CASTing of technical Al-Alloys under diffusive and magnetically controlled convective conditions) through the provision of the processed samples and by Hydro Aluminium Rolled Products GmbH, Germany (now Speira) for sample material delivery.

CONFLICT OF INTEREST

On behalf of all authors, the corresponding author states that there is no conflict of interest.

OPEN ACCESS

REFERENCES

1. D. Raabe, D. Ponge, P.J. Uggowitzer, M. Roscher, M. Paolantonio, C. Liu, H. Antrekowitsch, E. Kozeschnik, D. Seidmann, B. Gault, F. De Geuser, A. Deschamps, C. Hutchinson, and C. Liu, *Progr. Mater. Sci.* 128, 100947 (2022).
2. J. Taylor, The effect of iron in Al-Si casting alloys, in Casting Concepts, Adelaide, South Australia (2004).
3. D. Ferdian, C. Josse, P. Nguyen, N. Gey, N. Ratel-Ramond, P. de Parseval, Y. Thebault, B. Malard, J. Lacaze, and L. Salvo, *Metall. Mater. Trans. A* 46, 2814 (2015).
4. S. Steinbach, L. Ratke, G. Zimmermann, and O. Budenkova, *IOP Conf. Ser. Mater. Sci. Eng.* 117, 012019 (2016).
5. H. Zhang, M. Wu, C.M. Rodrigues, A. Ludwig, and A. Kharicha, *Metall. Mater. Trans. B* 52, 3007 (2021).
6. S.W. Hudson, D. Apelian, *Int. J. Metalcast.* 10, 289 (2016).
7. N. Rani, *J. Today's Ideas Tomorrow's Technol.* 5, 40 (2017).
8. N.E. Khalifa, M. Loey, and S. Mirjalili, *Artif. Intell. Rev.* 55, 2351 (2022).
9. A. Viardin, K. Nöth, M. Torabi Rad, and L. Sturz, *Automatic Detection of Equiaxed Dendrites Using Computer Vision Neural Networks* (Aachen, Germany, 2022).
10. K. He, G. Gkioxari, P. Dollar, and R. Girshick, Mask R-CNN (2018).
11. I. Arganda-Carreras, V. Kaynig, C. Rueden, K.W. Eliceiri, J. Schindelin, A. Cardona, and H. Sebastian-Seung, *Bioinformatics* 33, 2424 (2017).
12. J. Schindelin, I. Arganda-Carreras, E. Frise, V. Kaynig, M. Longair, T. Pietzsch, S. Preibisch, C. Rueden, S. Saalfeld, B. Schmid, J.Y. Tinevez, D.J. White, V. Hartenstein, K. Eliceiri, P. Tomancak, and A. Cardona, *Nat. Methods* 9, 676 (2012).
13. T. Enz, S. Steinbach, D. Simicic, G. Kasperovich, and L. Ratke, *Microgravity Sci. Technol.* 23, 345 (2011).
14. S. Steinbach, L. Ratke, *Metall. Mater. Trans. A* 38, 1388 (2007).